

Theoretical study of dynamical and electronic properties of noncentrosymmetric superconductor NbReSi

Surajit Basak ¹  and Andrzej Ptok ^{1,*} 

¹ Institute of Nuclear Physics, Polish Academy of Sciences, W. E. Radzikowskiego 152, PL-31342 Kraków, Poland; surajit.basak@ifj.edu.pl

* Correspondence: aptok@mmj.pl

Abstract: The noncentrosymmetric NbReSi superconductor with $T_c \simeq 6.5$ K is characterized by the relatively large upper critical magnetic field. Its multigap features were observed experimentally. Recent studies suggested realization of $P\bar{6}2m$ or $Ima2$ symmetry. We discuss the dynamical properties of both symmetries (e.g., phonon spectra). In this paper, using the *ab initio* techniques, we clarify this ambiguity, and conclude that the $Ima2$ symmetry is unstable, and $P\bar{6}2m$ should be realized. The $P\bar{6}2m$ symmetry is also stable in the presence of external hydrostatic pressure. We show that NbReSi with the $P\bar{6}2m$ symmetry should host phonon surface states for (100) and (110) surfaces. Additionally, we discuss the main electronic properties of the system with the stable symmetry.

Keywords: noncentrosymmetric superconductor; phonons; surface states; spin–orbit coupling

1. Introduction

Noncentrosymmetric superconductors are characterized by antisymmetric spin–orbit coupling (SOC) [1–3], which gives rise to the topological superconducting pairing as a result of a mixture of spin-singlet and spin-triplet components [3–5]. This behavior was first discovered in the heavy fermion compound CePt₃Si [6]. Recently, a large group of noncentrosymmetric superconductors have been discovered, e.g. Li₂(Pt_{1-x}Pd_x)₃B [7,8], BaPtSi₃ [9], LaNiC₂ [10], SrPtAs₂ [11], RPtSi ($R = \text{La, Ce, Pr, Nd, Sm, Gd}$) [12,13], A₂Cr₃As₃ ($A = \text{K, Rb, Cs}$) [14–16], K₂Mo₃As₃ [17], (Ta,Nb)Rh₂B₂ [18], ThTSi ($T = \text{Co, Ir, Ni, Pt}$) [19–21], or CeRh₂As₂ [22,23].

Recently many ternary noncentrosymmetric superconductors were discovered and studied. Typically, the $MM'Si$ class of materials (where M and M' are transition metals or rare earth metals) crystallise in several distinct structural symmetries, such as tetragonal $PbClF$ -type ($P4/nmm$ symmetry) [24], orthorhombic TiNiSi-type ($Pnma$ symmetry) [25], hexagonal ZrNiAl-type ($P\bar{6}2m$ symmetry) [26], or orthorhombic TiFeSi-type ($Ima2$ symmetry) [26]. Among the mentioned symmetries, two are noncentrosymmetric ($P\bar{6}2m$ and $Ima2$) and can give rise to unconventional triplet superconductivity. These types of features were discussed in the case of TaTSi ($T = \text{Re, Ru}$) [27,28] or TRuSi ($T = \text{Ti, Nb, Hf, Ta}$) [29], both with $Ima2$ symmetry.

In our paper, we focus on the recently studied noncentrosymmetric NbReSi superconductor [30], which exhibits superconducting properties below $T_c \simeq 6.5$ K [30–32]. A relatively large upper critical magnetic field was reported experimentally (around 12.5 T [31], 13.5 T [30], or 8.1 T [32]). The absence of spontaneous magnetic fields below T_c from muon-spin relaxation (μ SR) was observed [30]. The superfluid density and the spin-lattice relaxation rate suggest nodeless superconductivity [30]. The signatures of multigap superconductivity, evidenced by the field-dependent μ SR rate and the electronic specific heat coefficient [30] can be related to the multiband Fermi level [31].

However, the characterization of the studied samples suggest realization of the $P\bar{6}2m$ symmetry (cf. Ref. [30,31]) or $Ima2$ (cf. Ref. [32]) – structures presented in Fig. 1. We clarify this ambiguity using the *ab initio* techniques. From the study of dynamical properties, we claim



Citation: Basak, S.; Ptok, A.

Theoretical study of dynamical and electronic properties of noncentrosymmetric superconductor NbReSi. *Preprints* 2022, 1, 0. <https://doi.org/>

Publisher's Note: MDPI stays neutral with regard to jurisdictional claims in published maps and institutional affiliations.



Copyright: © 2022 by the authors. Licensee MDPI, Basel, Switzerland. This article is an open access article distributed under the terms and conditions of the Creative Commons Attribution (CC BY) license (<https://creativecommons.org/licenses/by/4.0/>).

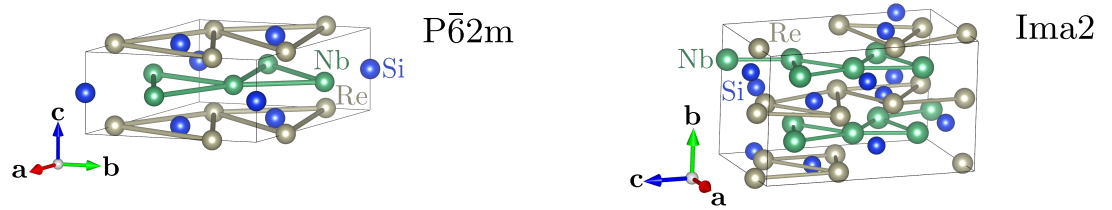


Figure 1. Schematic representation of NbReSi conventional cell with $P\bar{6}2m$ and $Ima2$ symmetries (as labeled). In both structures, the Re and Nb atoms form distorted kagome-like sublattices.

that the $P\bar{6}2m$ symmetry is stable in this system. We also discuss the dynamical and electronic properties of the system with stable symmetry.

The paper is organized as follows. Details of the techniques used are provided in Sec 2. Next, in Sec. 3 we present and discuss our theoretical results. Finally, a summary is provided in Sect. 4.

2. Calculation details

First-principles (DFT) calculations are performed using the projector augmented-wave (PAW) potentials [33] implemented in the Vienna Ab initio Simulation Package (VASP) code [34–36]. Calculations are made within the generalized gradient approximation (GGA) in the Perdew, Burke, and Ernzerhof (PBE) parameterization [37]. The calculations, including SOC, were performed with the energy cut-off set to 600 eV.

Initially, the crystal structure and atom positions were optimised. In the case of the $P\bar{6}2m$ symmetry, the primitive cell containing three formula units was optimized, with the $6 \times 6 \times 12$ k -point grid in the Monkhorst–Pack scheme [38]. Similarly, for the $Ima2$ symmetry, we used a conventional unit cell with $6 \times 6 \times 3$ k -point grid. As the convergence condition of an optimization loop, we take the energy difference of 10^{-5} eV and 10^{-7} eV for ionic and electronic degrees of freedom, respectively. Optimized structure parameters are collected in Sec. 3.1

The interatomic force constants (IFC) are calculated within the Parlinski-Li-Kawazoe method [39] implemented in PHONOPY package [40]. Force constants were obtained from first-principles calculations of the Hellmann–Feynman forces by VASP and used to build a dynamical matrix of the crystal. Phonon frequencies were obtained by diagonalization of the dynamical matrix. Calculations were performed using the supercell technique. In the case of the $P\bar{6}2m$ symmetry, the supercell based on $2 \times 2 \times 3$ primitive cells was used. For the $Ima2$ symmetry, we used a supercell based on $2 \times 1 \times 2$ conventional cells. In both cases, the reduced $3 \times 3 \times 3$ k -grid was used. Furthermore, dynamical properties were evaluated with ALAMODE software [41], using the multidisplacement method. Finally, to study the surface states of phonons, the surface Green’s function for a semi-infinite system [42] was calculated using WANNIERTOOLS [43].

3. Results and discussion

3.1. Crystal structure

After optimizing the crystal structures, we found:

- for the $P\bar{6}2m$ symmetry (space group No. 189): $a = b = 6.872$ Å, and $c = 3.310$ Å, while experimental values are $a = b = 6.719$ Å, and $c = 3.485$ Å [31]; Nb atoms are in Wyckoff positions $3g$: $(0.4020, 0, 1/2)$, Re atoms in Wyckoff positions $3f$: $(0.7411, 0, 0)$, while Si atoms in the two non-equivalent Wyckoff positions $2c$: $(1/3, 2/3, 0)$ and $1b$: $(0, 0, 1/2)$.
- for the $Ima2$ symmetry (space group No. 46): $a = 6.990$ Å, $b = 11.618$ Å, $c = 6.726$ Å, while the reported values are $a = 6.925$ Å, $b = 11.671$ Å, and $c = 6.694$ Å [32]; Nb atoms are

in three non-equivalent Wyckoff positions $4b$: $(1/4, 0.1959, 0.7093)$, $4b$: $(1/4, 0.7873, 0.7130)$ and $4a$: $(1/4, -0.0033, 0.0919)$, Re atoms in the two non-equivalent Wyckoff positions $4a$ $(0, 0, 0.7547)$ and $8c$: $(0.5344, 0.8732, 0.3776)$, while Si atoms in two non-equivalent positions $4b$: $(1/4, -0.0259, 0.4920)$ and $8c$: $(0.0037, 0.1677, 0.0064)$.

In the case of the $P\bar{6}2m$ symmetry, the primitive unit cell is equivalent to the conventional cell and contains three formula units. Contrary to this, for the $Ima2$ symmetry, the primitive cell contains six formula units, while the conventional one is twice bigger. The obtained crystal parameters are used in the next part of the paper as reference ones.

3.2. Dynamical properties

The phonon dispersions for both symmetries are presented in Fig. 2. Regardless of the symmetry, the phonon branches are collected into several groups separated by gaps. In the case of $P\bar{6}2m$ symmetry, acoustic modes exhibit a linear behavior around the Γ point. For the $Ima2$ symmetry, one of the acoustic modes along the $\Gamma-\Lambda_0$ path (continuing along the G_0-X path) poses the soft mode. However, this soft mode is also visible around the S-point. From the dynamical point of view, NbReSi is unstable with the $Ima2$ symmetry.

In both symmetries, Re and Nb atoms form distorted kagome-like sublattices (see Fig. 1), and should exist a relation between these two structures. In fact, there is a group-subgroup relationship between the discussed symmetries [44], which is, $P\bar{6}2m \rightarrow Amm2 \rightarrow Ima2$. This

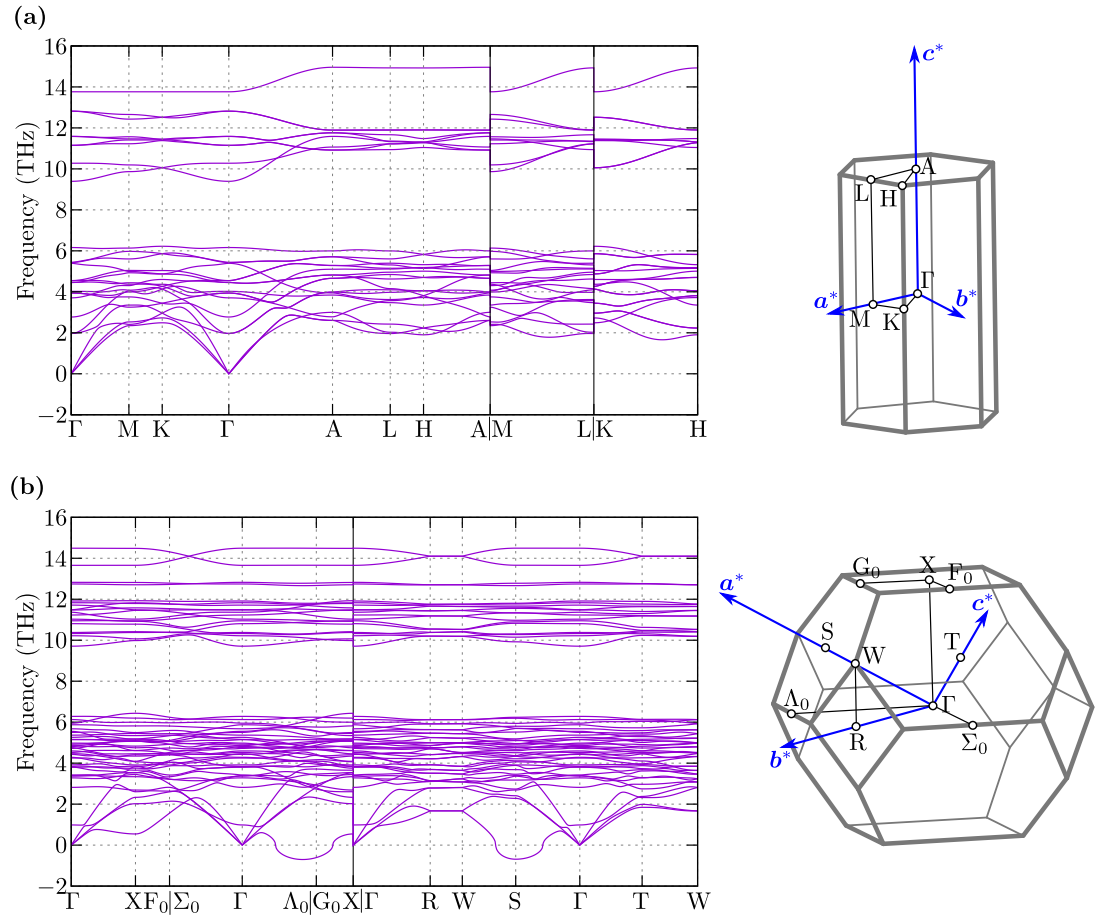


Figure 2. The phonon dispersion along high symmetry directions (left panels) and the Brillouin zone (right panels) for $P\bar{6}2m$ and $Ima2$ (top and bottom panels, respectively).

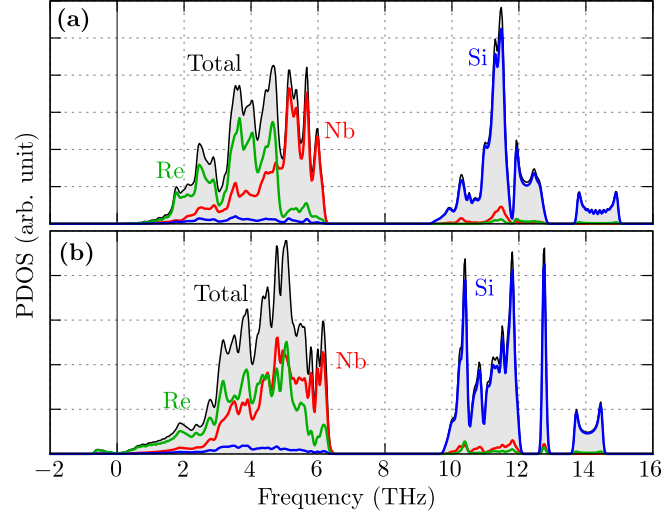


Figure 3. The phonon density of states (PDOS) for $P\bar{6}2m$ and $Ima2$ (top and bottom panels, respectively).

allows $Ima2$ to emerge from $P\bar{6}2m$ as a consequence of atom displacements. Nevertheless, $P\bar{6}2m$ is stable and does not exhibit any soft modes that can lead to $Amm2$ or $Ima2$ symmetries.

The above mentioned properties are also reflected in the phonon density of states (PDOS), presented in Fig. 3. A more precise analysis uncovers the contribution of separate atoms in vibration modes. The lower-frequency modes are realized by Re and Nb atoms (relatively heavy atoms). As can be expected, high-frequency modes are realized by lighter atoms, i.e. Si. The PDOS are qualitatively comparable for both symmetries. As we can see, the soft mode in the $Ima2$ structure is realized by vibrations of Nb atoms.

The irreducible representations of the phonon modes at the Γ point are given as [45]:

- for the $P\bar{6}2m$ symmetry:

$$\begin{aligned}\Gamma_{\text{acoustic}} &= A_2'' + E' \\ \Gamma_{\text{optic}} &= 2A_1' + 2A_2' + A_1'' + 3A_2'' + 6E' + 2E'',\end{aligned}\quad (1)$$

where $A_2'' + E'$ modes are infra-red active, while $E' + E''$ modes are Raman active.

- for the $Ima2$ symmetry:

$$\begin{aligned}\Gamma_{\text{acoustic}} &= A_1 + B_1 + B_2 \\ \Gamma_{\text{optic}} &= 14A_1 + 11A_2 + 11B_1 + 15B_2,\end{aligned}\quad (2)$$

where $A_1 + B_1 + B_2$ modes are infra-red active, while $A_1 + A_2 + B_1 + B_2$ modes are Raman active.

For lower symmetry (i.e. $Ima2$), in practice all modes are Raman active. Here we should note that in both symmetries primitive cells contain different numbers of atoms. As a consequence, the Raman spectra can be used as a tool to confirm the symmetry realized by NbReSi.

Phonon surface states

Realization of hexagonal symmetry by NbReSi can give rise to phonon surface states [46]. The calculated surface Green functions are presented in Fig. 4. The phonon dispersion (Fig. 2) is very complex and concentrated in the low frequency range (below 7.5 THz). However, for surfaces (100) and (110), the phonon edge states are clearly visible at several places. For example, at the \bar{L} point, where the phonon surface states are realized by separated modes with

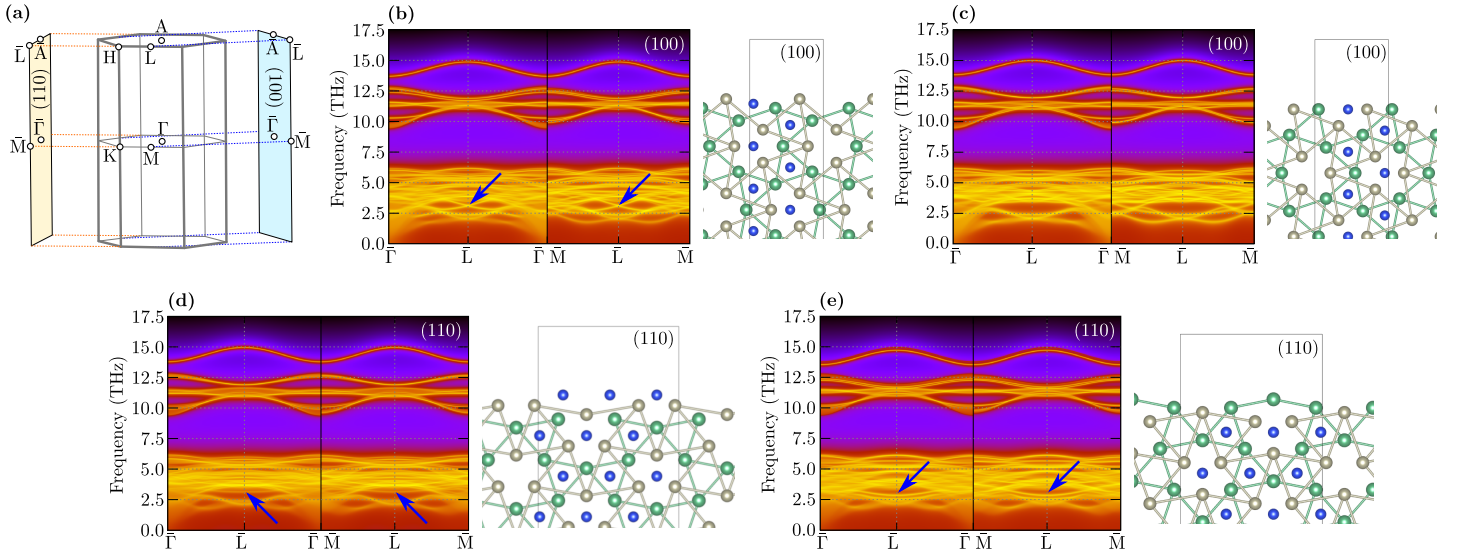


Figure 4. Projection of the 3D bulk Brillouin zone on the 2D surface Brillouin zones for (100) and (110) surfaces (a). Panels (b)–(e) present surface Green functions for different surfaces (as labeled) and corresponding terminations (right schemats). Blue arrows show phonon surface states at \bar{L} point.

relatively large intensity (marked by blue arrows in Fig. 4). Interestingly, for some terminations, this mode is not realized, see Fig. 4(c).

The relatively small frequencies of the mentioned phonon surface modes suggest their strong connection with Nb or Re atoms on the surface. For the surface (100), where the bulk M and Γ points are projected on the surface $\bar{\Gamma}$ point, we observed a Dirac-like structure (Fig. 4(b)). A more precise analysis of the surface band structure uncovers avoided crossing of two edge states. Contrary to this, for the (110) surface, where bulk K and M points are projected on the surface \bar{M} point, while bulk K and Γ points are projected on surface $\bar{\Gamma}$ point, we observed only one separated surface state (Fig. 4(c) and Fig. 4(d)).

Role of hydrostatic pressure

Now we briefly discuss the impact of external hydrostatic pressure on NbReSi. Under external pressure, the volume of the system decreases monotonically (Fig. 5(a)). In the absence of pressure, the energy for both symmetries is comparable. However, comparison of their volumes (per formula unit, see Fig. 5(a)) clearly show that the unit cell of $P\bar{6}2m$ is always more dense. This feature has an important impact under external pressure and indicates a smaller enthalpy (i.e., the sum of the ground states energy and pV terms) of the system with $P\bar{6}2m$ than $Ima2$. Furthermore, above some pressure (around 20 GPa), the system with the $Ima2$ symmetry was impossible to optimize, and the structure goes to the $P\bar{6}2m$ symmetry. This suggests instability of the NbReSi system with the $Ima2$ symmetry even under pressure.

Fig. 5(b) shows the dispersion curves for the $P\bar{6}2m$ symmetry under pressure 30 GPa, which are comparable with the one obtained in the ambient pressure (i.e. Fig. 2(a)). The range of realized phonon frequencies increase under pressure, as a result of the decreased volume of the system. Nevertheless, the system is stable and does not exhibit phonon softening.

3.3. Electronic properties

Now, we briefly describe the electronic properties of the NbReSi system with stable the $P\bar{6}2m$ symmetry. The obtained electronic band structure (Fig. 6) is in agreement with the initial one presented in Ref. [31].

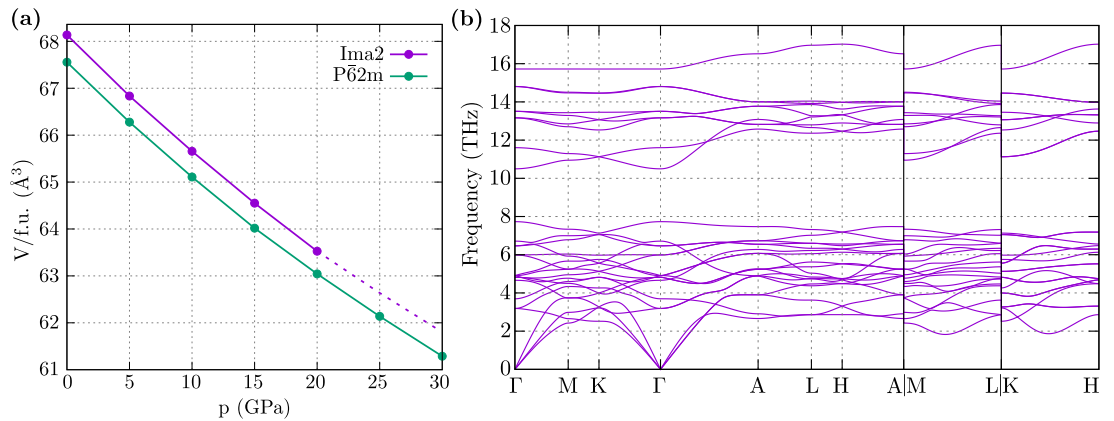


Figure 5. Influence of external hydrostatic pressure on NbReSi. (a) Pressure dependence of the unit cell volume (per formula unit) for system with P6̄2m and Ima2 symmetries (as labeled). (b) Phonon dispersion curves for system with P6̄2m under pressure 30 GPa.

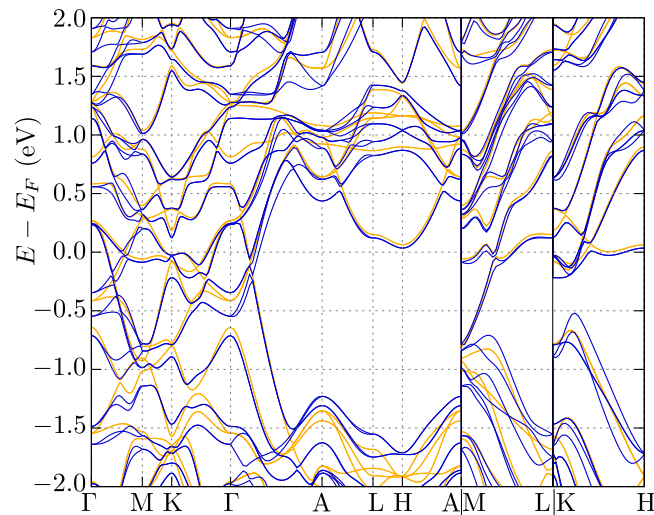


Figure 6. The electronic band structure along high symmetry directions for the P6̄2m symmetry in the absence and presence of spin-orbit coupling (orange and blue lines, respectively).

The SOC band splitting near the Fermi level is estimated to be 180 meV. This is a relatively high value of the SOC in comparison to the other noncentrosymmetric superconductors [3], suggesting the realization of topological superconductivity in NbReSi. A significant role of the antisymmetric SOC is well visible along the c direction (e.g., the M–L or K–H paths in Fig. 6). A large SOC is observed in the $k_z = 0$ plane (e.g. along the Γ –M–K– Γ path), in contrast to a relatively suppressed value of the SOC for $k_z = \pi/c$ (e.g. along the A–L–H–A).

The Fermi surface is presented in Fig. 7. In the absence of SOC, the Fermi surface is composed of three pockets. Introduction of the SOC leads to band decoupling, whereas the Fermi surface preserves the shape unchanged qualitatively. Surprisingly, the Fermi surface exhibits quasi-one-dimensional features (i.e., the Fermi surface pocket are given by relatively flat pieces for $k_z = \text{const.}$, see Fig. 7(b)).

The features of the electronic band structure, as well as the Fermi surface topology, make NbReSi very similar to the $A_2\text{Cr}_3\text{As}_3$ ($A = \text{K, Rb, Cs}$) [47–50] and $\text{K}_2\text{Mo}_3\text{As}_3$ [50,51] compounds. NbReSi does not exhibit any magnetic order features (the ground state is nonmagnetic), while mentioned $A_2\text{Cr}_3\text{As}_3$ poses magnetic order [52]. Regardless of this, the electronic band struc-

ture at $k_z = \pi/c$ is characterized by a relatively large gap, which was observed in both cases. For NbReSi, the states around the Fermi level are mostly composed of Re-5*d* and Nb-4*d* orbitals [31], while for $A_2Cr_3As_3$, Cr-3*d* orbitals have the greatest contribution [47]. The Fermi surface of NbReSi is very similar to $A_2Cr_3As_3$ [47–50] or $K_2Mo_3As_3$ [50,51] (both cases with $P\bar{6}2m$ symmetry).

Here we should mention that despite having the same symmetry, the two structures possess different intrinsic features: e.g., $A_2Cr_3As_3$ contains quasi-one-dimensional chain of Cr atoms along the *c* direction, while NbReSi has layers of distorted kagome-like sublattice of Nb and Re atoms in the *ab* plane (see Fig. 1). This causes detailed differences in the electronic band structure. Quasi-one-dimensional chains in $A_2Cr_3As_3$ are related to the nearly flat bands within the *ab* plane and a strong k_z dependence of the electron dispersion. In NbReSi, too, we observe strong k_z -dependence of the electron dispersion. Additionally, the absence of characteristic band structure features for the kagome-like structure is observed (i.e. absence of the flat bands). This can be related to the relatively large distances between atoms in the distorted kagome-like planes (3.63 Å and 4.47 Å for Nb–Nb and Re–Re pairs, respectively; cf. Fig. 1).

The smaller distance between the atoms is related to the bonding between Re and Si (distance around 2.43 Å), and can have a relatively strong impact on the electronic properties. Indeed, the charge density distribution analyses (not presented) provide signature of a strong bonding within these pairs. Such a structure with a strong bonding between the atoms along *c* can be responsible for the quasi-one-dimensional character of NbReSi visible on the Fermi surface.

4. Summary and conclusions

We discussed the basic properties of the recently experimentally studied noncentrosymmetric superconductor NbReSi. The experiments suggest realization of the $P\bar{6}2m$ symmetry (cf. Ref. [30,31]) or *Ima2* (cf. Ref. [32]) symmetry. Using the *ab initio* technique, we show that NbReSi is stable with the $P\bar{6}2m$ symmetry, while the *Ima2* phase exhibits (imaginary) phonon soft modes. This can be verified in a relatively simple way by the Raman scattering measurements. The NbReSi with the $P\bar{6}2m$ symmetry is stable also under hydrostatic pressure. We also found that the phonon surface states can be realized by NbReSi with the $P\bar{6}2m$ symmetry, for (100) and (110) surfaces.

NbReSi with stable the $P\bar{6}2m$ symmetry exhibits the electronic band structure and the Fermi surface very similar to quasi-one-dimensional $A_2Cr_3As_3$ [53]. Surprisingly, the Fermi surface of NbReSi uncovers quasi-one-dimensional features, which can be associated with the realization of quasi-one-dimensional chains of Re–Si, with a strong bonding between the atoms. Additionally, the relatively large value of spin–orbit coupling, as well as similarities to

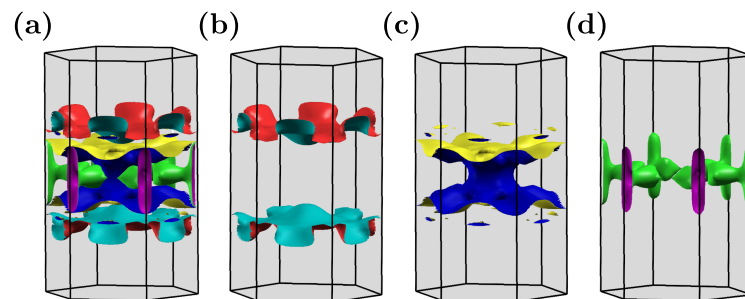


Figure 7. The Fermi surface for the $P\bar{6}2m$ symmetry (in the absence of spin–orbit coupling). Panel (a) presents the total Fermi surface, while panels (b)–(d) show separated pockets.

$A_2Cr_3As_3$ promote this compound as a good candidate for the realization of unconventional superconductivity.

Author Contributions: A.P. initialized this project; S.B. and A.P. realized theoretical calculations; A.P. prepared the first version of the manuscript. All authors have read and agreed to the published version of the manuscript.

Funding: This work was supported by National Science Centre (NCN, Poland) under Projects No. 2021/43/B/ST3/02166 (A.P.).

Institutional Review Board Statement: Not applicable

Informed Consent Statement: Not applicable

Data Availability Statement: Not applicable

Acknowledgments: Some figures in this work were rendered using VESTA [54]. A.P. appreciates funding in the framework of scholarships of the Minister of Science and Higher Education (Poland) for outstanding young scientists (2019 edition, No. 818/STYP/14/2019).

Conflicts of Interest: The authors declare no conflict of interest.

References

1. Yip, S. Noncentrosymmetric Superconductors. *Annu. Rev. Condens. Matter Phys.* **2014**, *5*, 15. <https://doi.org/10.1146/annurev-conmatphys-031113-133912>.
2. Zhang, X.; Liu, J.; Liu, F. Topological Superconductivity Based on Antisymmetric Spin–Orbit Coupling. *Nano Lett.* **2022**. <https://doi.org/10.1021/acs.nanolett.2c03213>.
3. Smidman, M.; Salamon, M.B.; Yuan, H.Q.; Agterberg, D.F. Superconductivity and spin–orbit coupling in non-centrosymmetric materials: a review. *Rep. Prog. Phys.* **2017**, *80*, 036501. <https://doi.org/10.1088/1361-6633/80/3/036501>.
4. Gor'kov, L.P.; Rashba, E.I. Superconducting 2D System with Lifted Spin Degeneracy: Mixed Singlet-Triplet State. *Phys. Rev. Lett.* **2001**, *87*, 037004. <https://doi.org/10.1103/PhysRevLett.87.037004>.
5. Ptok, A.; Rodríguez, K.; Kacpia, K.J. Superconducting monolayer deposited on substrate: Effects of the spin-orbit coupling induced by proximity effects. *Phys. Rev. Materials* **2018**, *2*, 024801. <https://doi.org/10.1103/PhysRevMaterials.2.024801>.
6. Bauer, E.; Hilscher, G.; Michor, H.; Paul, C.; Scheidt, E.W.; Griбанov, A.; Seropegin, Y.; Noël, H.; Sigrist, M.; Rogl, P. Heavy Fermion Superconductivity and Magnetic Order in Noncentrosymmetric $CePt_3Si$. *Phys. Rev. Lett.* **2004**, *92*, 027003. <https://doi.org/10.1103/PhysRevLett.92.027003>.
7. Togano, K.; Badica, P.; Nakamori, Y.; Orimo, S.; Takeya, H.; Hirata, K. Superconductivity in the Metal Rich Li-Pd-B Ternary Boride. *Phys. Rev. Lett.* **2004**, *93*, 247004. <https://doi.org/10.1103/PhysRevLett.93.247004>.
8. Yuan, H.Q.; Agterberg, D.F.; Hayashi, N.; Badica, P.; Vandervelde, D.; Togano, K.; Sigrist, M.; Salamon, M.B. S-Wave Spin-Triplet Order in Superconductors without Inversion Symmetry: Li_2Pd_3B and Li_2Pt_3B . *Phys. Rev. Lett.* **2006**, *97*, 017006. <https://doi.org/10.1103/PhysRevLett.97.017006>.
9. Bauer, E.; Khan, R.T.; Michor, H.; Royanian, E.; Grytsiv, A.; Melnychenko-Koblyuk, N.; Rogl, P.; Reith, D.; Podloucky, R.; Scheidt, E.W.; et al. $BaPtSi_3$: A noncentrosymmetric BCS-like superconductor. *Phys. Rev. B* **2009**, *80*, 064504. <https://doi.org/10.1103/PhysRevB.80.064504>.
10. Bonalde, I.; Ribeiro, R.L.; Syu, K.J.; Sung, H.H.; Lee, W.H. Nodal gap structure in the noncentrosymmetric superconductor $LaNiC_2$ from magnetic-penetration-depth measurements. *New J. Phys.* **2011**, *13*, 123022. <https://doi.org/10.1088/1367-2630/13/12/123022>.
11. Nishikubo, Y.; Kudo, K.; Nohara, M. Superconductivity in the Honeycomb-Lattice Pnictide $SrPtAs$. *J. Phys. Soc. Jpn.* **2011**, *80*, 055002. <https://doi.org/10.1143/JPSJ.80.055002>.
12. Klepp, K.; Parthé, E. RPTi phases ($R = La, Ce, Pr, Nd, Sm$ and Gd) with an ordered $ThSi_2$ derivative structure. *Acta Crystallogr. B* **1982**, *38*, 1105. <https://doi.org/10.1107/S056774088200507X>.
13. Kneidinger, F.; Michor, H.; Sidorenko, A.; Bauer, E.; Zeiringer, I.; Rogl, P.; Blaas-Schenner, C.; Reith, D.; Podloucky, R. Synthesis, characterization, electronic structure, and phonon properties of the noncentrosymmetric superconductor $LaPtSi$. *Phys. Rev. B* **2013**, *88*, 104508. <https://doi.org/10.1103/PhysRevB.88.104508>.
14. Bao, J.K.; Liu, J.Y.; Ma, C.W.; Meng, Z.H.; Tang, Z.T.; Sun, Y.L.; Zhai, H.F.; Jiang, H.; Bai, H.; Feng, C.M.; et al. Superconductivity in Quasi-One-Dimensional $K_2Cr_3As_3$ with Significant Electron Correlations. *Phys. Rev. X* **2015**, *5*, 011013. <https://doi.org/10.1103/PhysRevX.5.011013>.

15. Tang, Z.T.; Bao, J.K.; Liu, Y.; Sun, Y.L.; Ablimit, A.; Zhai, H.F.; Jiang, H.; Feng, C.M.; Xu, Z.A.; Cao, G.H. Unconventional superconductivity in quasi-one-dimensional $\text{Rb}_2\text{Cr}_3\text{As}_3$. *Phys. Rev. B* **2015**, *91*, 020506. <https://doi.org/10.1103/PhysRevB.91.020506>.
16. Tang, Z.T.; Bao, J.K.; Wang, Z.; Bai, H.; Jiang, H.; Liu, Y.; Zhai, H.F.; Feng, C.M.; Xu, Z.A.; Cao, G.H. Superconductivity in quasi-one-dimensional $\text{Cs}_2\text{Cr}_3\text{As}_3$ with large interchain distance. *Sci. China Mater.* **2015**, *58*, 16. <https://doi.org/10.1007/s40843-015-0021-x>.
17. Mu, Q.G.; Ruan, B.B.; Zhao, K.; Pan, B.J.; Liu, T.; Shan, L.; Chen, G.F.; Ren, Z.A. Superconductivity at 10.4 K in a novel quasi-one-dimensional ternary molybdenum pnictide $\text{K}_2\text{Mo}_3\text{As}_3$. *Sci. Bull.* **2018**, *63*, 952. <https://doi.org/10.1016/j.scib.2018.06.011>.
18. Carnicom, E.M.; Xie, W.; Klimczuk, T.; Lin, J.; Górnicka, K.; Sobczak, Z.; Ong, N.P.; Cava, R.J. TaRh_2B_2 and NbRh_2B_2 : Superconductors with a chiral noncentrosymmetric crystal structure. *Sci. Adv.* **2018**, *4*, eaar7969. <https://doi.org/10.1126/sciadv.aar7969>.
19. Domieracki, K.; Kaczorowski, D. Superconductivity in a non-centrosymmetric compound ThCoSi . *J. Alloys Compd.* **2016**, *688*, 206. <https://doi.org/10.1016/j.jallcom.2016.06.292>.
20. Domieracki, K.; Kaczorowski, D. Superconductivity in non-centrosymmetric ThNiSi . *J. Alloys Compd.* **2018**, *731*, 64. <https://doi.org/10.1016/j.jallcom.2017.10.004>.
21. Ptok, A.; Domieracki, K.; Kapcia, K.J.; Łażewski, J.; Jochym, P.T.; Sternik, M.; Piekarz, P.; Kaczorowski, D. Electronic and lattice properties of noncentrosymmetric superconductors ThTSi ($T = \text{Co, Ir, Ni, and Pt}$). *Phys. Rev. B* **2019**, *100*, 165130. <https://doi.org/10.1103/PhysRevB.100.165130>.
22. Khim, S.; Landaeta, J.F.; Banda, J.; Bannor, N.; Brando, M.; Brydon, P.M.R.; Hafner, D.; Küchler, R.; Cardoso-Gil, R.; Stockert, U.; et al. Field-induced transition within the superconducting state of CeRh_2As_2 . *Science* **2021**, *373*, 1012. <https://doi.org/10.1126/science.abe7518>.
23. Ptok, A.; Kapcia, K.J.; Jochym, P.T.; Łażewski, J.; Oleś, A.M.; Piekarz, P. Electronic and dynamical properties of CeRh_2As_2 : Role of Rh_2As_2 layers and expected orbital order. *Phys. Rev. B* **2021**, *104*, L041109. <https://doi.org/10.1103/PhysRevB.104.L041109>.
24. Welter, R.; Venturini, G.; Malaman, B.; Ressouche, E. Crystallographic data and magnetic properties of new RTX compounds ($R = \text{La-Sm, Gd}$; $T = \text{Ru, Os}$; $X = \text{Si, Ge}$). Magnetic structure of NdRuSi . *J. Alloys Compd.* **1993**, *202*, 165. [https://doi.org/10.1016/0925-8388\(93\)90536-V](https://doi.org/10.1016/0925-8388(93)90536-V).
25. Morozkin, A.; Seropegin, Y.; Sviridov, I.; Riabinkin, I. Crystallographic data of new ternary Co_2Si -type RTSi ($R = \text{Y, Tb-Tm}$, $T = \text{Mn, Ru}$) compounds. *J. Alloys Compd.* **1999**, *282*, L4–L5. [https://doi.org/10.1016/S0925-8388\(98\)00784-1](https://doi.org/10.1016/S0925-8388(98)00784-1).
26. Subba Rao, G.V.; Wagner, K.; Balakrishnan, G.; Janaki, J.; Paulus, W.; Schöllhorn, R.; Subramanian, V.S.; Poppe, U. Structure and superconductivity studies on ternary equiatomic silicides, $\text{MM}'\text{Si}$. *Bull. Mater. Sci.* **1985**, *7*, 215. <https://doi.org/10.1007/BF02747575>.
27. Sajilesh K. P.; Singh, R.P. Superconducting properties of the non-centrosymmetric superconductors TaXSi ($X = \text{Re, Ru}$). *Supercond. Sci. Technol.* **2021**, *34*, 055003. <https://doi.org/10.1088/1361-6668/abe4b7>.
28. Sharma, S.; Sajilesh K. P.; Richards, A.D.S.; Gautreau, J.; Pula, M.; Beare, J.; Kojima, K.M.; Yoon, S.; Cai, Y.; Kushwaha, R.K.; et al. Role of spin orbital coupling in unconventional superconductivity, 2022, [arXiv:2209.09852]. <https://doi.org/10.48550/arXiv.2209.09852>.
29. Shang, T.; Zhao, J.; Hu, L.H.; Ma, J.; Gawryluk, D.J.; Zhu, X.; Zhang, H.; Zhen, Z.; Yu, B.; Xu, Y.; et al. Unconventional superconductivity in topological Kramers nodal-line semimetals. *Sci. Adv.* **2022**, *8*, eabq6589. <https://doi.org/10.1126/sciadv.abq6589>.
30. Shang, T.; Tay, D.; Su, H.; Yuan, H.Q.; Shiroka, T. Evidence of fully gapped superconductivity in NbReSi : A combined μSR and NMR study. *Phys. Rev. B* **2022**, *105*, 144506. <https://doi.org/10.1103/PhysRevB.105.144506>.
31. Su, H.; Shang, T.; Du, F.; Chen, C.F.; Ye, H.Q.; Lu, X.; Cao, C.; Smidman, M.; Yuan, H.Q. NbReSi : A noncentrosymmetric superconductor with large upper critical field. *Phys. Rev. Materials* **2021**, *5*, 114802. <https://doi.org/10.1103/PhysRevMaterials.5.114802>.
32. Sajilesh, K.P.; Motla, K.; Meena, P.K.; Kataria, A.; Patra, C.; K., S.; Hillier, A.D.; Singh, R.P. Superconductivity in noncentrosymmetric NbReSi investigated by muon spin rotation and relaxation. *Phys. Rev. B* **2022**, *105*, 094523. <https://doi.org/10.1103/PhysRevB.105.094523>.
33. Blöchl, P.E. Projector augmented-wave method. *Phys. Rev. B* **1994**, *50*, 17953. <https://doi.org/10.1103/PhysRevB.50.17953>.
34. Kresse, G.; Hafner, J. Ab initio molecular-dynamics simulation of the liquid-metal–amorphous-semiconductor transition in germanium. *Phys. Rev. B* **1994**, *49*, 14251. <https://doi.org/10.1103/PhysRevB.49.14251>.
35. Kresse, G.; Furthmüller, J. Efficient iterative schemes for ab initio total-energy calculations using a plane-wave basis set. *Phys. Rev. B* **1996**, *54*, 11169. <https://doi.org/10.1103/PhysRevB.54.11169>.
36. Kresse, G.; Joubert, D. From ultrasoft pseudopotentials to the projector augmented-wave method. *Phys. Rev. B* **1999**, *59*, 1758. <https://doi.org/10.1103/PhysRevB.59.1758>.
37. Perdew, J.P.; Burke, K.; Ernzerhof, M. Generalized Gradient Approximation Made Simple. *Phys. Rev. Lett.* **1996**, *77*, 3865. <https://doi.org/10.1103/PhysRevLett.77.3865>.
38. Monkhorst, H.J.; Pack, J.D. Special points for Brillouin-zone integrations. *Phys. Rev. B* **1976**, *13*, 5188. <https://doi.org/10.1103/PhysRevB.13.5188>.
39. Parlinski, K.; Li, Z.Q.; Kawazoe, Y. First-Principles Determination of the Soft Mode in Cubic ZrO_2 . *Phys. Rev. Lett.* **1997**, *78*, 4063. <https://doi.org/10.1103/PhysRevLett.78.4063>.
40. Togo, A.; Tanaka, I. First principles phonon calculations in materials science. *Scr. Mater.* **2015**, *108*, 1. <https://doi.org/10.1016/j.scriptamat.2015.07.021>.

41. Tadano, T.; Gohda, Y.; Tsuneyuki, S. Anharmonic force constants extracted from first-principles molecular dynamics: applications to heat transfer simulations. *J. Phys.: Condens. Matter* **2014**, *26*, 225402. <https://doi.org/10.1088/0953-8984/26/22/225402>.
42. Sancho, M.P.L.; Sancho, J.M.L.; Sancho, J.M.L.; Rubio, J. Highly convergent schemes for the calculation of bulk and surface Green functions. *J. Phys. F: Met. Phys.* **1985**, *15*, 851. <https://doi.org/10.1088/0305-4608/15/4/009>.
43. Wu, Q.S.; Zhang, S.N.; Song, H.F.; Troyer, M.; Soluyanov, A.A. WANNIERTOOLS: An open-source software package for novel topological materials. *Comput. Phys. Commun.* **2018**, *224*, 405. <https://doi.org/10.1016/j.cpc.2017.09.033>.
44. Ivantchev, S.; Kroumova, E.; Madariaga, G.; Pérez-Mato, J.M.; Aroyo, M.I. SUBGROUPGRAPH: a computer program for analysis of group-subgroup relations between space groups. *J. Appl. Cryst.* **2000**, *33*, 1190. <https://doi.org/10.1107/S0021889800007135>.
45. Kroumova, E.; Aroyo, M.I.; Perez-Mato, J.M.; Kirov, A.; Capillas, C.; Ivantchev, S.; Wondratschek, H. Bilbao Crystallographic Server : Useful Databases and Tools for Phase-Transition Studies. *Phase Transitions* **2003**, *76*, 155. <https://doi.org/10.1080/0141159031000076110>.
46. Li, J.; Wang, L.; Liu, J.; Li, R.; Zhang, Z.; Chen, X.Q. Topological phonons in graphene. *Phys. Rev. B* **2020**, *101*, 081403. <https://doi.org/10.1103/PhysRevB.101.081403>.
47. Jiang, H.; Cao, G.; Cao, C. Electronic structure of quasi-one-dimensional superconductor $K_2Cr_3As_3$ from first-principles calculations. *Sci. Rep.* **2015**, *5*, 16054. <https://doi.org/10.1038/srep16054>.
48. Cuono, G.; Autieri, C.; Forte, F.; Mercaldo, M.T.; Romano, A.; Avella, A.; Noce, C. A minimal tight-binding model for the quasi-one-dimensional superconductor $K_2Cr_3As_3$. *New J. Phys.* **2019**, *21*, 063027. <https://doi.org/10.1088/1367-2630/ab2489>.
49. Xu, C.; Wu, N.; Zhi, G.X.; Lei, B.H.; Duan, X.; Ning, F.; Cao, C.; Chen, Q. Coexistence of nontrivial topological properties and strong ferromagnetic fluctuations in quasi-one-dimensional $A_2Cr_3As_3$. *npj Comput. Mater.* **2020**, *6*, 30. <https://doi.org/10.1038/s41524-020-0294-9>.
50. Taddei, K.M.; Lei, B.H.; Susner, M.A.; Zhai, H.F.; Bullard, T.J.; Sanjeeva, L.D.; Zheng, Q.; Sefat, A.S.; Chi, S.; dela Cruz, C.; et al. Gapless spin-excitations in the superconducting state of a quasi-one-dimensional spin-triplet superconductor, 2022, [arXiv:2206.11757]. <https://doi.org/10.48550/arXiv.2206.11757>.
51. Yang, Y.; Feng, S.Q.; Lu, H.Y.; Wang, W.S.; Chen, Z.P. Electronic Structures of Newly Discovered Quasi-One-Dimensional Superconductors $A_2Mo_3As_3$ ($A = K, Rb, Cs$). *J. Supercond. Nov. Magn.* **2019**, *32*, 2421. <https://doi.org/10.1007/s10948-019-5054-z>.
52. Wu, X.X.; Le, C.C.; Yuan, J.; Fan, H.; Hu, J.P. Magnetism in Quasi-One-Dimensional $A_2Cr_3As_3$ ($A = K, Rb$) Superconductors. *Chinese Phys. Lett.* **2015**, *32*, 057401. <https://doi.org/10.1088/0256-307X/32/5/057401>.
53. Wu, X.; Yang, F.; Le, C.; Fan, H.; Hu, J. Triplet p_z -wave pairing in quasi-one-dimensional $A_2Cr_3As_3$ superconductors ($A = K, Rb, Cs$). *Phys. Rev. B* **2015**, *92*, 104511. <https://doi.org/10.1103/PhysRevB.92.104511>.
54. Momma, K.; Izumi, F. VESTA3 for three-dimensional visualization of crystal, volumetric and morphology data. *J. Appl. Crystallogr.* **2011**, *44*, 1272. <https://doi.org/10.1107/S0021889811038970>.